



Interactive Diffraction from Biological Nanostructures

D. S. Dhillon¹, J. Teyssier², M. Single¹, I. Gaponenko², M. C. Milinkovitch³ and M. Zwicker¹

¹Computer Graphics Group, Institute of Computer Science and Applied Mathematics, University of Bern, Bern, Switzerland
djdhillon@gmail.com, michael.single@students.unibe.ch, zwicker@iam.unibe.ch

²DMPC, University of Geneva, Geneva 4, Switzerland
jeremie.teyssier@unige.ch, iaroslav.gaponenko@unige.ch

³Department of Genetics and Evolution, Laboratory of Artificial and Natural Evolution (LANE), University of Geneva, Geneva, Switzerland
michel.milinkovitch@unige.ch

Abstract

We describe a technique for interactive rendering of diffraction effects produced by biological nanostructures, such as snake skin surface gratings. Our approach uses imagery from atomic force microscopy that accurately captures the geometry of the nanostructures responsible for structural colouration, that is, colouration due to wave interference, in a variety of animals. We develop a rendering technique that constructs bidirectional reflection distribution functions (BRDFs) directly from the measured data and leverages pre-computation to achieve interactive performance. We demonstrate results of our approach using various shapes of the surface grating nanostructures. Finally, we evaluate the accuracy of our pre-computation-based technique and compare to a reference BRDF construction technique

Keywords: structural colors, diffraction, wave effects, physically based rendering, BRDF, natural gratings, biological iridescence, real-time rendering

ACM CCS: I.3.7 [Computer Graphics]: Three-Dimensional Graphics and Realism Colour, shading, shadowing and texture

1. Introduction

In biology, structural colouration is the production of colour through the interaction of light with nanoscale surface structures or intracellular submicron photonic crystals. Colour production is due to wave interference with quasiperiodic structures whose periodicity leads to interaction with visible light. The interference may be created by a variety of photonic mechanisms, such as diffraction gratings (see nanostructures in Figure 1), 2D and 3D photonic crystals or crystal fibers. The connection between microscopic structures and colouration have been observed by Robert Hooke as early as in the seventeenth century, and the discovery of the wave nature of light led to the conclusion that the cause for the colouration lies in wave interference. Structural colours have been described in a variety of plants as well as invertebrate and vertebrate animals. Spectacular examples include the vivid and sometimes iridescent colours of some insects' wings and integument, bird feathers and reptile scales (see Figure 2). A number of researchers have investigated the rendering of structural colours for computer graphics purposes. Most of these techniques, however, are either too slow for interactive rendering, or rely on simplifying assumptions to achieve real-time performance.

In this paper, we derive reflectance models for interactive rendering directly from physical measurements of biological structures. We show that our approach is more accurate than previous methods which rely on simplifying assumptions about the nanostructures. In particular, our approach applies to surfaces with quasiperiodic structures at the nanometre scale that can be represented as height fields. Such structures are found on the skin of snakes, wings of butterflies or the bodies of various insects. We focus on snake skins, and we acquired nanoscale height fields of different snake sheds using atomic force microscopy (AFM).

The pioneering work of Stam [Sta99] shows how to directly formulate bidirectional reflection distribution functions (BRDFs) in terms of nanoscale height fields of the acquired surfaces, although this formulation is not immediately suitable for interactive rendering. Instead, we develop a technique to pre-compute lookup tables that allow us to efficiently evaluate the BRDF and achieve real-time performance. We demonstrate our approach using nanostructures acquired from the sheds of two snake species, *Elaphe guttata* (*Pantherophis guttatus*) and *Xenopeltis unicolor* (see Figure 2), which exhibit moderate and intense iridescence of the skin, respectively.

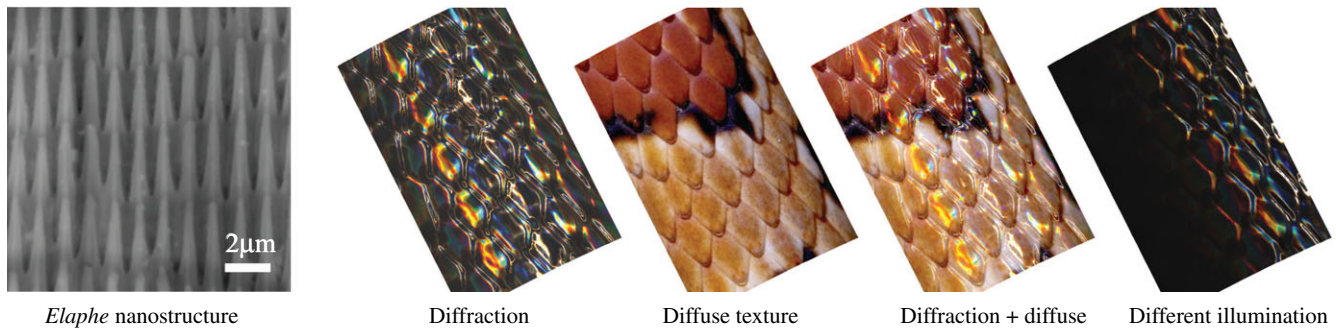


Figure 1: We render diffraction from snake skin surface gratings directly based on the surface nanostructures. We show a surface nanostructure of an *Elaphe* snake on the left, and rendering with and without texture under different illumination directions.



Figure 2: *Xenopeltis* snakes exhibit spectacular structural colours [Xen].

We also show results of our technique using an idealized grating and the pits on a CD surface. We verify our technique by comparing with measured reflectance properties of the snake sheds, and analytic properties of idealized gratings. In summary, our main contributions are

- A method to render structural colours due to diffraction gratings directly based on physical measurements.
- An algorithm for interactive rendering leveraging pre-computed lookup tables.

2. Previous Work

Structural colours are generated through interference of light waves. In the computer graphics literature, Stam [Sta99] was the first to develop reflection models based on wave optics, called ‘diffraction shaders’, that can produce colourful diffraction effects. His approach is based on a far field approximation and the Kirchhoff integral, and he shows that for surfaces represented as nanoscale height fields it is possible to derive their BRDF as the Fourier transform of a function of the height field. This formulation, however, is not immediately useful for efficient rendering of measured, complex nanostructures, since this would require the on-the-fly evaluation of and integration

over Fourier transforms of the height field that depend on the light and viewing geometry. Instead, Stam derives analytic BRDFs for a restricted class of height fields that can be modelled as probabilistic superposition of bumps forming ‘periodic-like’ structures, such as the pits on the surface of compact disks. Biological nanostructures, however, are more complex and do not lend themselves to this simplified statistical model based on a Gaussian approximation of a homogeneous random function.

Following Stam’s pioneering work there were a number of efforts to model wave effects in computer graphics. Cuypers *et al.* [CHB*12] proposed ‘wave-based BSDFs’ (WBSDFs). At the core of their approach are Wigner distribution functions (WDFs), which can be understood to represent complex wavefronts as series of plane waves with real-valued, potentially negative amplitudes. Cuypers *et al.* formulate a wave rendering equation that relates the reflected (or transmitted) wavefront to the incoming wavefront and the WDF of the surface structure. Since the wave rendering equation consists of the same recursive hemispherical integrals as the rendering equation, it is straightforward to adapt conventional Monte Carlo renderers to solve it. The main advantage of WBSDFs over Stam’s diffraction shaders is that they capture near field effects, which appear when the receiving surface is within a few wavelengths to the diffractive surface. A disadvantage is that the WDF of a 2D surface nanostructure is a 4D function. For interactive rendering this is unattractive, and Cuypers *et al.* demonstrate their approach using separable nanostructures that can be represented by two 2D lookup tables. Recently, Wu *et al.* [WZ13] proposed a *microfacet scattering metric* based BRDF model that incorporates WDF for interactive rendering of diffraction effects from multiple bounces. Their BRDF model exploits the Gaussian distribution properties of the microfacet normals to achieve interactive speeds. Since our goal is interactive rendering of diffraction directly based on complex measured 2D nanostructures with *height bumps* of unknown distributions, we derive our method from Stam’s diffraction shaders.

Other approaches to capture wave effects in computer graphics include optical path differences (OPD) [TFNC01, ZCG08], where one keeps track of distances that rays travel to calculate their phase shifts, and augmented light fields [OKG*10], which also employ WDFs. Recently, Musbach *et al.* [MMRO13] even described a finite difference time domain (FDTD) algorithm to simulate the

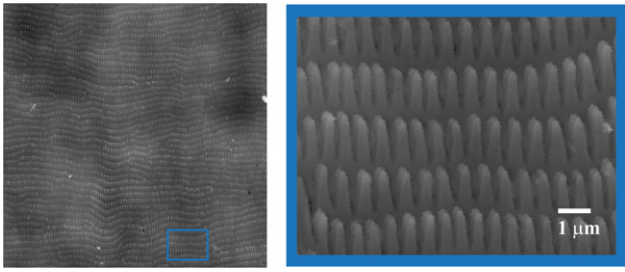


Figure 3: The surface nanostructure of the shed of a *Xenopeltis unicolor* snake obtained using atomic force microscopy (AFM).

propagation of electromagnetic energy based on Maxwell's equations, targeted at computer graphics applications. All these methods are unsuitable for interactive rendering, although in principle it should be possible to use them to pre-compute 4D BRDF lookup tables.

Lindsay and Agu [LA06] propose a technique targeted at interactive rendering where diffractive BRDFs are pre-computed and stored using spherical harmonics. Since this approach is limited to low order spherical harmonics, it may be inappropriate for BRDFs produced by complex biological nanostructures. Also Imura et al. [IOS*09] focus on interactive rendering. Their method is based on storing textures representing OPDs to compute interference. While this approach is generic and can be used for interference due to thin films, multilayer materials and diffraction gratings, their approach stores only one OPD at each surface location. This is too simplistic to model complex nanostructures, and they only show results of a diffraction grating with uniformly spaced pits. Finally, Sun [Sun06] describes a method for interactive rendering of biological iridescences, but his approach is restricted to multilayer thin films.

3. Overview

The goal of our approach is interactive rendering of diffraction effects from complex physical nanostructures acquired using electron or AFM. We obtained snake skin surface gratings geometry using AFM, which delivers height field data representing surface structures at the nanometre scale. We will denote such height fields as $h(x, y)$. Figure 3 shows an example of a shed of a sunbeam snake (*Xenopeltis unicolor*), a non-venomous species known for its spectacular iridescent scales.

The nanostructures we are interested in exhibit periodicity on the scale of the wavelength of visible light. Hence, rendering requires taking into account the wave nature of light to reproduce these effects. Stam [Sta99] has shown, however, that it is possible to formulate conventional BRDFs for such nanostructures under certain assumptions. In particular, Stam assumes that the surface is observed from a large enough distance and then uses the Kirchhoff integral [BS63] to derive the BRDF.

Let us denote BRDFs using the notation $BRDF_{\lambda}(\omega_i, \omega_r)$ where, λ represents a specific wavelength, and ω_i and ω_r are the incident and reflected direction vectors, both understood as unit vectors pointing

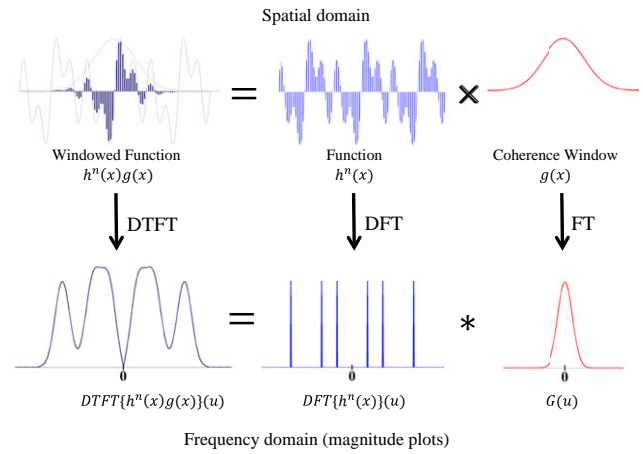


Figure 4: The DTFT of a bandlimited signal $h^n(x)$ windowed with $g(x)$ equals the convolution of its DFT and the Fourier transform of the windowing function.

away from the surface. For a height field $h(x, y)$, Stam's formulation defines an auxiliary function

$$p(x, y) = e^{i w k h(x, y)}, \quad (1)$$

where $w = -(\cos \theta_i + \cos \theta_r)$ with θ_i and θ_r being the angles of incident and reflected directions with the surface normal, and the wavenumber is $k = 2\pi/\lambda$. The BRDF of a nanostructure can then be written using the Fourier transform $P(u, v) = \mathfrak{F}\{p(x, y)\}(u, v)$,

$$BRDF_{\lambda}(\omega_i, \omega_r) = \frac{F^2 G}{\lambda^2 A w^2} \left\langle \left| P\left(\frac{u}{\lambda}, \frac{v}{\lambda}\right) \right|^2 \right\rangle, \quad (2)$$

where F represents the Fresnel term, u, v, w are computed from the incident and reflected directions as $(u, v, w)^T = -\omega_i - \omega_r$, $\langle X \rangle$ represents the expected value of a random variable X , and A is an area of integration on the surface that is considered to contribute to diffraction. Note that the region of integration is physically limited and it acts as a 'window' on $p(x, y)$. Thus, the power of the Fourier transform $|P|^2$ is also proportional to the area A , and the area factor cancels out. Finally, G is a geometry term,

$$G = \frac{(1 + \omega_i \cdot \omega_r)^2}{\cos \theta_i \cos \theta_r}.$$

4. Efficient Evaluation for Discrete Nanostructures

In this section, we introduce our approach for interactive rendering of complex measured nanostructures represented as discrete height fields. Conceptually, we simply obtain the BRDF for a discrete height field by replacing the Fourier transform of a continuous height

field with a *discrete time Fourier transform* (DTFT), which is the continuous Fourier transform of a discrete signal,

$$BRDF_{\lambda}(\omega_i, \omega_r) = \frac{F^2 G}{\lambda^2 A w^2} \left| T_0^2 P_{DTFT} \left(\frac{u}{\lambda}, \frac{v}{\lambda} \right) \right|^2, \quad (3)$$

where P_{DTFT} denotes the DTFT of p , and T_0 is the sampling distance for the discretization of $p(x, y)$, given equal and uniform sampling in both directions. If we assume that the continuous height field is bandlimited and sampled sufficiently, the DTFT consists of non-overlapping replicas of the continuous spectrum. Hence, for frequencies $u/\lambda, v/\lambda$ within the bandlimit of the continuous height field, $T_0^2 P_{DTFT}(u/\lambda, v/\lambda) = P(u/\lambda, v/\lambda)$, and the discretization is exact. We also assume that the integration area is large enough such that a discretized patch sufficiently captures the statistics of the complete height field. Therefore, we use the Fourier transform directly, instead of treating it as a random variable and using its expected value.

Finally, we work with BRDFs normalized by reflectance at normal incidence for convenience. We introduce a term $C(\omega_i, \omega_r)$ that subsumes normalization and the factor $F^2 G/\lambda^2 A w^2$ to simplify notation, that is,

$$BRDF_{\lambda}(\omega_i, \omega_r) = C(\omega_i, \omega_r) \left| P_{DTFT} \left(\frac{u}{\lambda}, \frac{v}{\lambda} \right) \right|^2, \quad (4)$$

and $C(\omega_i, \omega_r) = F^2 G/F_0^2 w^2$, where F_0 is the Fresnel term for normal incident light and viewing directions along the surface normal.

4.1. Taylor Series Expansion

The BRDF in Equation (3) is not suitable for direct evaluation because p and its DTFT P_{DTFT} are functions of the height field and w (see Equation 1), which is given by the light and viewing directions. To be able to pre-compute and tabulate the Fourier transforms of p , we use a Taylor series expansion of the exponential in $p(x, y)$ over the variable w ,

$$p(x, y) = \sum_{n=0}^{\infty} \frac{1}{n!} (i w k)^n h^n(x, y). \quad (5)$$

While the Taylor series converges in theory, we use a finite number N of terms depending on an upper-bound on error in estimating the exponential in Equation (1). Now the DTFT consists of a sum

$$P_{DTFT} \left(\frac{u}{\lambda}, \frac{v}{\lambda} \right) = \sum_{n=0}^N \frac{1}{n!} (w k)^n \mathfrak{F}_n \left(\frac{u}{\lambda}, \frac{v}{\lambda} \right), \quad (6)$$

where each summand includes a DTFT,

$$\mathfrak{F}_n \left(\frac{u}{\lambda}, \frac{v}{\lambda} \right) = \text{DTFT} \{ i^n h^n(x, y) \} \left(\frac{u}{\lambda}, \frac{v}{\lambda} \right). \quad (7)$$

The main idea of our approach for efficient rendering is to pre-compute the DTFTs \mathfrak{F}_n and evaluate the Taylor series expansion in a shader. We will discuss implementation details in Section 5.

4.2. Coherence Length and Windowing

The BRDF formulation derived by Stam (Equation 2) that we adapt for our approach requires integrating the electro-magnetic radiation at the point of reflection over a region on the surface. Since most sources emit light with limited *coherence length*, the surface area over which incident wavefronts produce diffraction is limited. We assume a coherence length of $65\mu\text{m}$ since sunlight typically has coherence length on the second order of the wavelength [MGFG12]. We model this aspect by introducing a spatial windowing function implemented as a Gaussian with variance $4\sigma_s = 65\mu\text{m}$.

Note that spatial windowing results in a convolution in the Fourier domain, which allows us to replace the DTFT in our formulation with the discrete Fourier transform (DFT). The DFT of a discrete height field patch is equivalent to the DTFT of an infinitely periodic function consisting of replicas of the same discrete patch. By windowing with a window function that is zero outside the central replica, the convolution of either the DFT or the DTFT of the height field with the Fourier transform of the window become equivalent, see Figure 4. Hence, we replace the DTFT in Equation (7) with the DFT and obtain

$$\mathfrak{F}_n \left(\frac{u}{\lambda}, \frac{v}{\lambda} \right) = \sum_{s,t} \text{DFT} \{ i^n h^n(x, y) \} (s, t) G \left(\frac{u}{\lambda} - \phi_s, \frac{v}{\lambda} - \psi_t \right), \quad (8)$$

where we sum over the coefficients s, t of the DFT, ϕ_s, ψ_t denote the non-zero frequencies of the DFT, and the Fourier transform of the Gaussian window is

$$G(u, v) = \exp \left(-\frac{u^2 + v^2}{2\sigma_f^2} \right), \quad \sigma_f = 1/(2\pi\sigma_s).$$

4.3. Spectral Rendering

We would like to be able to represent incident illumination using accurate spectra. Hence, we include the integration over the colour spectrum to compute CIE XYZ outputs in our pre-computation framework. For brevity we consider only the X colour channel here, and a similar derivation can be applied for the Y and Z channels. Using the BRDF formulation from Equation (4), and given an incident direction ω_i and spectral power distribution of the illumination $S(\lambda)$, the X channel of the reflected light in direction ω_r is

$$X = C(\omega_i, \omega_r) \cos \theta_i \int_{\lambda} \left| P_{DTFT} \left(\frac{u}{\lambda}, \frac{v}{\lambda} \right) \right|^2 S_x(\lambda) d\lambda, \quad (9)$$

where, for convenience, we define $S_x(\lambda) = S(\lambda)\bar{x}(\lambda)$, and \bar{x} is a CIE XYZ colour matching function. Here, we assume that the Fresnel terms are constant over λ and thus $C(\omega_i, \omega_r)$ can be moved out of the integration. This is a reasonable choice for keratin-based outer epidermis layers on animal skins.

Substituting the Taylor series expansion of Equation (6) in Equation (9) gives us

$$X = C(\omega_i, \omega_r) \cos \theta_i \sum_{p=0}^{2N} w^p I_p(u, v), \quad (10)$$

where

$$I_p(u, v) = \sum_{\substack{n = \max(0, p - N), \\ m = p - n}}^{\min(p, N)} \frac{1}{n!m!} \int_{\lambda} \left(\frac{2\pi}{\lambda}\right)^p \mathfrak{D}_m^n\left(\frac{u}{\lambda}, \frac{v}{\lambda}\right) S_x(\lambda) d\lambda, \quad (11)$$

and $\mathfrak{D}_m^n(u/\lambda, v/\lambda)$ is the dot product of the complex Fourier transform values expressed as 2-element vectors, that is,

$$\mathfrak{D}_m^n\left(\frac{u}{\lambda}, \frac{v}{\lambda}\right) = \mathfrak{F}_n\left(\frac{u}{\lambda}, \frac{v}{\lambda}\right) \bullet \mathfrak{F}_m\left(\frac{u}{\lambda}, \frac{v}{\lambda}\right). \quad (12)$$

We calculate the terms \mathfrak{F}_n and \mathfrak{F}_m using the windowed DFT as in Equation (8).

We pre-compute and tabulate $I_p(u, v)$, $p \in [0, 2N]$, by performing numerical integration for the integral in Equation (11) for discrete values of (u, v) . We discuss the discretization of the u - v space in Section 5 along with other implementation details. The resulting lookup tables are loaded and used by our shader to perform summation in Equation (10) on-the-fly and thus compute the resulting RGB colours. Computation of $I_p(u, v)$ is the most time-consuming task for our shader and pre-computing it allows us to achieve interactive performance.

5. Implementation and Data Acquisition

We have implemented two OpenGL Shading Language (GLSL) fragment shaders for our approach; one with direct computations and high accuracy for reference, and another with lookup tables for high interactivity. The reference shader performs an on-the-fly numerical integration for the integral in Equation (9) using the Trapezoidal rule with uniform discretization of the λ dimension at a resolution of 5 nm. To compute the P_{DFT} terms it uses pre-computed DFTs for the Taylor terms given in Equation (8). Summation in Equation (8) is performed for each discrete λ value using a window large enough to span $4\sigma_f$ in both dimensions. To compute DFT tables, we generally use given nanostructure height fields that span at least $65 \mu\text{m}^2$ and are sampled with resolution of at least 100 nm. This ensures that the spectral response encompasses all the wavelengths in the visible spectrum, i.e. (380–780 nm). While the reference shader is not interactive, it is used for comparative evaluations as discussed in Section 7.

The lookup shader uses a pre-computed set of lookup tables for the $I_p(u, v)$ terms as explained in Section 4.3. We generate one lookup table for each value of p in Equation (10) by discretizing the u - v space, which spans $(u, v) \in [-2, 2] \times [-2, 2]$ by definition. Equation (11) shows that u - v space is mapped non-uniformly, due to λ , to the frequency domain, which is uniformly discretized when computing DFT coefficients. For a given (u, v) , uniform discretization of λ implies compressing sampled frequencies to the region near the origin (of the frequency domain). Furthermore, for natural nanostructures, most of their spectral energy lies at lower spatial frequencies, which map closer to region near $(u, v) = (0, 0)$ than the higher frequencies. We thus choose to discretize u - v space non-linearly by drawing more samples in the region near $(u, v) = (0, 0)$. For this, we pre-compute $I_p(u, v)$ at discrete locations $(2u_i^a \text{sign}(u_i), 2v_i^a \text{sign}(v_i))$ where a is a constant power term

and (u_i, v_i) uniformly discretizes the space $[-1, 1] \times [-1, 1]$ at a given resolution. Section 7 shows differences in computed BRDFs for linear and non-linear discretizations. The non-linear discretization is akin to *importance sampling* of the BRDF. The value of a was empirically set to 5. We use 29–79 lookup tables (corresponding to 15–40 Taylor terms) of resolution up to 501×501 . We discuss the performance and behaviour of the lookup shader in Section 7.

We used Schlick's approximation to compute Fresnel terms. We fixed the refractive index at 1.5 since this value is close to the measured value from snake sheds. We scale our BRDF values using a shadowing function given by Cook and Torrance [CT82] since most of the grooves in the snake skin nanostructures would form a V-cavity along the plane for a wavefront with their top-edges at almost the same height.

Most of the diffraction effects for our data sets are present in the lower part of the intensity range. So we scale-up the intensity of the incident illumination and perform gamma correction. For convenience, we define 1 *RU* (relative unit) as the equivalent of intensity of light incident normally on a mirror-surface to just saturate the shader output to white colour. We used a scaling factor in the range (100–2000)*RU* for our BRDF visualizations.

Data Acquisition: To extract the true surface topography as shown in Figures 1 and 3, we glued a single snake scale on a metal disc covered with carbon adhesive tape. Then, measurements were carried out using intermittent contact mode in a Bruker Dimension 3100 atomic force microscope under ambient conditions, using a Nanoscope V controller. The tips used were etched silicon TESP tips with a nominal frequency and force constant of 320 kHz and 42 N/m, respectively.

6. Evaluation

In this section we provide a detailed evaluation of our approach. In Section 6.1, we verify that our approach is consistent with analytic properties of idealized gratings. In Section 6.2, we compare our results to real diffraction patterns from snake skins, and in Section 6.3 to Stam's original formulation.

6.1. Virtual Test Bench

In order to check the physical reliability of our method, we used it as a virtual diffraction experimental bench on: (i) a synthetic blazed grating, and (ii) nanostructures on *Elaphe* & *Xenopeltis* snake skin sheds, shown in Figure 5. When light at a wavelength λ falls on a sample presenting a periodicity a along the incident plane, under an incident angle θ to the normal of the surface (Figure 6), the angle ϕ corresponding to the direction of the emerging beam showing constructive interferences at maximum intensity is given by

$$\sin \theta = \sin \phi + m\lambda/a, \quad (13)$$

where m is the order of diffraction [PLT05]. Figure 7 shows fits of first order ($m = 1$) diffraction angles of idealized periodic structures (with their periodicity a as the free parameter) to data generated with our method, using an illumination angle $\theta = 75^\circ$. Each graph in

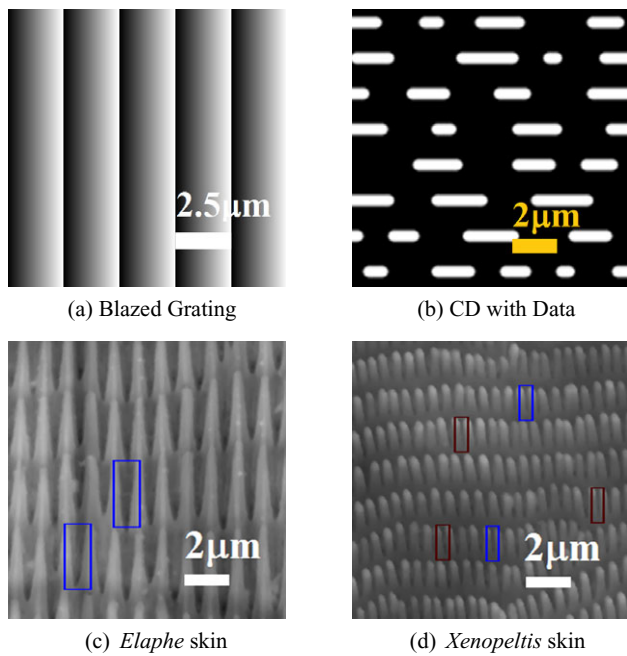


Figure 5: Various nanostructures used by our shader, each of size $12.5\mu\text{m}^2$. These are close-ups and we use larger patches for rendering.

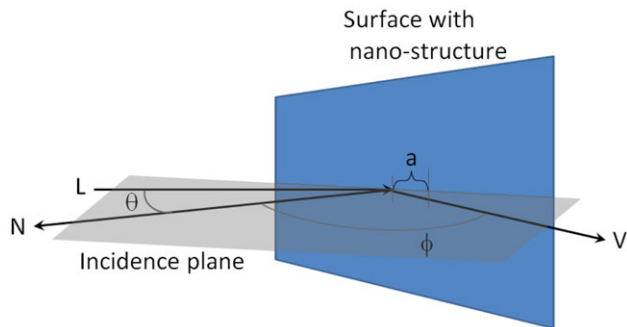


Figure 6: Virtual test bench. L is the light direction, V is the viewing direction and N is the surface normal. a represents the periodicity of a grating.

Figure 7 shows: (i) reflectance of the nanostructure as computed by our method, (ii) viewing angles for peak reflectances of the nanostructure at each wavelength (solid red curves), and (iii) diffraction angles for an idealized periodic structure with certain periodicity a according to Equation (13) (one or more dotted curves). We estimate periodicities a from ‘peak viewing angles’ and report them in Table 1 along with estimated variances, and they match well with our structures in Figure 5. The dotted and solid curves are closely overlapping in Figures 7(a)-(c). For the blazed grating and *Elaphe*, there is strong diffraction only in one direction. For *Xenopeltis*, there is strong diffraction in two directions, namely *along* and *across* the finger-like structures.

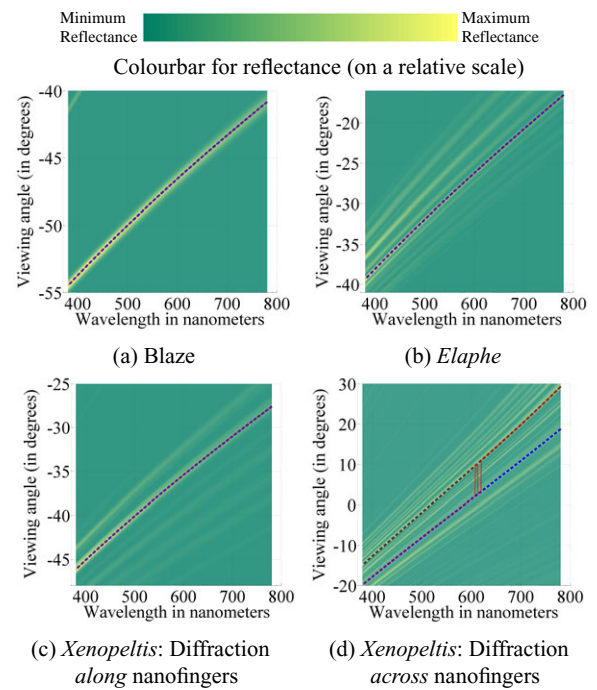


Figure 7: We plot reflectances obtained using our BRDFs at different viewing angles over visible wavelengths. The BRDFs exhibit typical ‘peak-viewing-angles’ corresponding to idealized periodic structures with matching periodicities. The colourbar at the top visualizes the relative scale for reflectance for all the plots from (a) to (d).

Table 1: Periodicity estimated for different nanostructures using our method.

Data	Estimated Periodicity	
	mean (in nm)	variance (in nm)
Blazed grating (2500 nm)	2500.34	0.16
<i>Elaphe</i>	1144.28	0.15
<i>Xenopeltis</i> (along nanofingers)	1552.27	0.45
<i>Xenopeltis</i> (across nanofingers)		
- Blue curve in Figure 7(d)	605.89	0.12
- Brown curve in Figure 7(d)	536.13	0.04

Note that in Figure 7(d) for *Xenopeltis* we see multiple yellow lines in the reflectance image, corresponding to different periodicities. This is because multiple sub-regions of the nanostructure have slightly different periodicities. Two such periodicities have higher reflectance than others and the ‘peak-viewing angle’ toggles between them. We plot diffraction angles for both periodicities in dotted curves and show representative sub-regions in Figure 5(d) with boxes of same colours. Similarly, we illustrate representative regions for estimated periodicity a for *Elaphe* in Figure 5(c). Our method exhibits similar good fits for higher order diffraction modes.

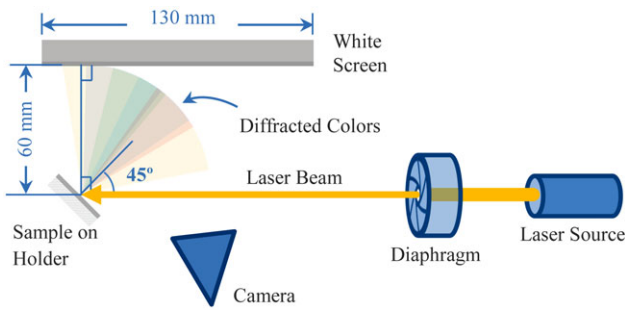


Figure 8: Schematic diagram for the experimental setup used for verification.

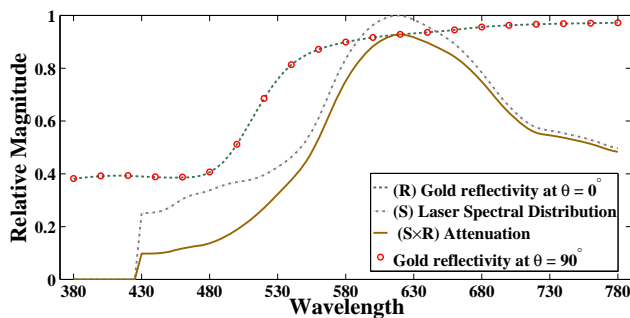


Figure 9: Spectral power distribution for the laser beam used and reflectivity for gold plating (on relative scales). Let θ represent the angle between the incident beam and a viewing direction. For $\theta \leq 90^\circ$, the profile for gold's reflectivity versus wavelength changes only negligibly.

6.2. Experimental Verification

We validate our method qualitatively against real-world snake skin diffraction under controlled conditions. Figure 8 illustrates our experimental setup. A nanostructure sample of about $5 \times 5 \text{ mm}^2$ is mounted vertically on a holder and illuminated with a broad-spectrum supercontinuum laser (Fianium SC450-6) beam of known power distribution (see Figure 9). The laser beam travels horizontally, falls exactly at 45° on the sample, and gets reflected onto a vertical white screen which is set parallel to the output laser-beam. The reflections off the screen are captured using a Nikon D800 in a raw format. We simulate these geometric conditions in our renderer while ignoring minor keystone distortion between the screen and the camera plane as this does not affect our qualitative comparisons. The laser beam passes through a diaphragm's aperture of about $100 \mu\text{m}$ in diameter. To protect the sample from damage by the laser-beam, we cover it with a thin uniform coating of gold. The gold layer has reflectance properties which vary considerably across the wave-spectrum. Though a gold film with thickness of only a few nanometres may transmit a fraction of incident light energy as suggested by Loebich [Loe72], for simplicity we treat it as an opaque layer. This simplification explains some tonal differences between our renderings and the actual images. We profiled the Fresnel term for gold with the approximation suggested by Lazányi et al. [LSK05] using gold's complex refractive index profile [Gol13].

We found only a weak angular dependence for gold reflectivity for our setup. We thus include a wavelength dependent Fresnel-term as part of the integrand in Equation (9) while pre-computing the lookup tables. We replicate all specified optical conditions in our simulations as well. Finally, we average BRDF responses over a small neighbourhood in the $u-v$ space since each (viewed) pixel subtends a small solid angle (cone) at the viewpoint.

Figure 10 shows three images captured from our experimental setup for *Elaphe* and *Xenopeltis* skin samples under different exposures and orientations and white balanced for CIE D65 daylight. It also shows the output of our lookup shader under similar conditions. Our renderings of the *Elaphe* skin sample under high illumination shows both, the primary (central) band of colours as well as the secondary (other) bands of colours corresponding to different modes of diffraction. We observe some fine radial colour streaks, known as *speckle patterns*, emanating away from the central highlight in the photographs (see inset for Figure 10 b). Such *speckle effects* may arise due to randomly distributed static scattering elements in the path of a coherent beam and are difficult to reproduce exactly. To a certain degree, this randomness (in the height bumps) is captured by our AFM microscope and it is present in our height field data. Thus, our simulations produce similar streaks (see inset for Figure 10e), albeit somewhat thicker and blurred due to averaging in $u-v$ space (see previous paragraph). Scanning higher resolution height fields would allow us to better reproduce these *speckle effects*. Overall, the rendered colour patterns are similar in form and appearance to those observed in corresponding actual images. Similarly, our simulation for *Xenopeltis* produces colour patterns which are qualitatively similar to those observed in the actual image.

6.3. Comparison with Stam

Since our method is derived from Stam's diffraction shader approach [Sta99], we discuss in detail why our extension is necessary to obtain more accurate BRDFs for complex nanostructures, such as our snake skin samples. Stam makes a general assumption about surface height fields being homogeneous random functions, such that the BRDFs can be computed using their correlation functions. He then provides implementations for two specific cases, namely: (a) periodic-like structures and (b) Gaussian random functions. For an experimental comparison with our approach and the observed diffraction patterns, we employ both of Stam's implementations for our *Elaphe* sample under the same geometric and optical conditions as in Figure 10(a).

For periodic-like structures, Stam models the height fields as made up of 'bumps' whose geometry is known analytically, and which are distributed either in a uniformly periodic manner or following a Poisson distribution. For such a height field, one can derive an analytical expression for the BRDF. In a simplistic approach to directly employ Stam's method for snake skin nanostructures, for both *Elaphe* and *Xenopeltis* we regard the 'nanofingers' as 'bumps', which are repeated regularly along both axes. With these assumptions and estimated periodicities of the nanofingers for the *Elaphe* sample, we run an implementation of Equations (21)–(24) in Stam's paper [Sta99]. Following are the implementation details along with results.

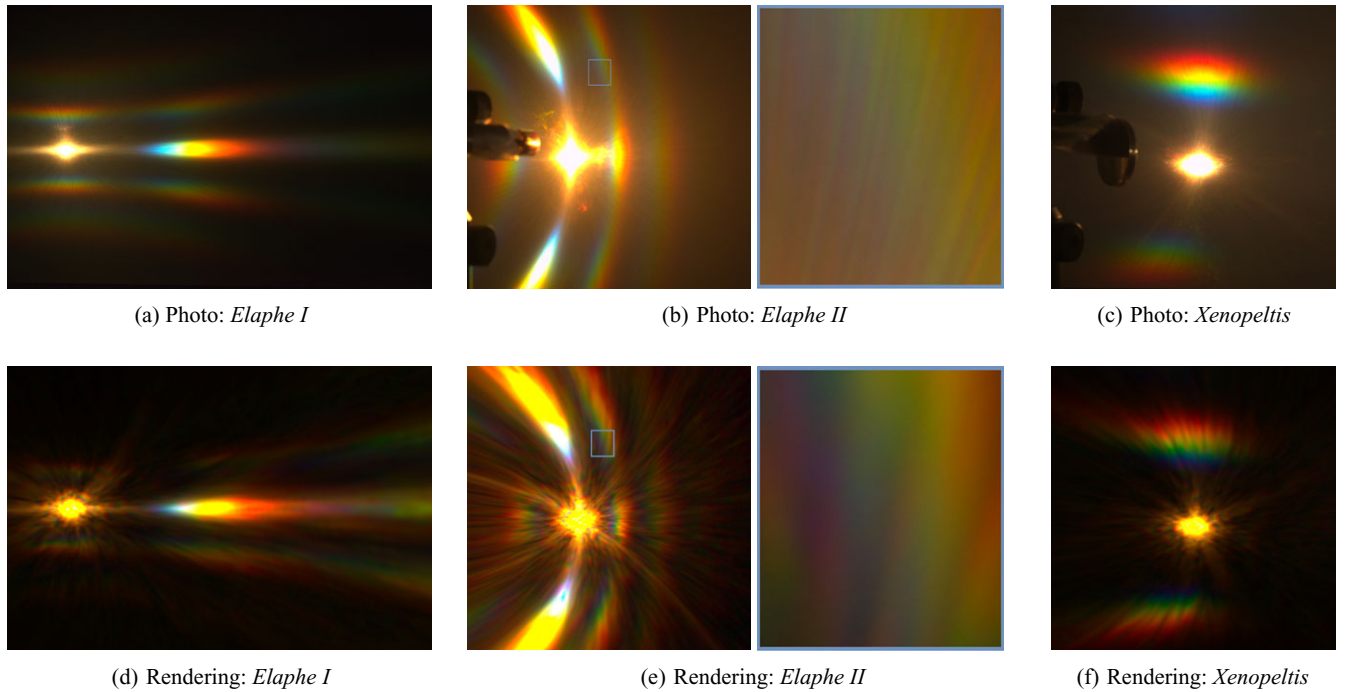


Figure 10: (a)–(c) Three photos from our experimental setup and (d)–(f) corresponding simulation results for our shader. (a)–(b) and (d)–(e) An Elaphe sample at different exposures and orthogonal orientations. (c) and (f) A Xenopeltis sample.

Unlike Stam, we assume a regular arrangement along the Y axis instead of a Poisson distribution. This results in a product of two delta functions inside the summation in Equation (21) in Stam’s paper [Sta99]. The spectral density in our case is thus given as

$$S_p(u, v, \lambda) = \lambda^2 \sum_{n=-\infty}^{\infty} \sum_{m=-\infty}^{\infty} |\varphi(n, m)|^2 \delta(u - n\lambda/\Delta x) \times \delta(v - m\lambda/\Delta y), \quad (14)$$

where

$$\varphi(n, m) = \frac{a^2 b^2}{\Delta x^2 \Delta y^2} |\Phi(2\pi na/\Delta x, 2\pi mb/\Delta y)|^2. \quad (15)$$

Please refer to Stam’s paper [Sta99] for details of the terms used here. Both the delta functions in Equation (14) must be non-zero for a given wavelength to contribute to the BRDF. We use the first delta function to find wavelengths that make it non-zero, and then select those wavelengths for which m is within a small absolute ϵ -bound from an integer value. This step is then repeated for the other delta function. Only the selected wavelengths contribute to the spectral density. Figure 11 shows results for different values of ϵ and for different ‘bump’ profiles. Figure 11(a) shows the pattern obtained with $\epsilon = 0.01$ for a rectangular ‘bump’, which does not exhibit continuous horizontal bands of colours. Increasing the ϵ threshold produces these bands, but also a vertical band, see Figure 11(b), which was not observed in our experimental setup even at very long exposures. These renderings are qualitatively different from

the observation shown in Figure 10(a). Also, Figure 11(c) shows that using a different (triangular) ‘bump’ only changes the relative intensity of the colours, but it does not significantly change the diffraction pattern and does not produce a better match.

For the second case of Stam’s method, we assume that we can model our nanostructure as a Gaussian random function. We implemented the formulation in Equation (12) in Stam’s paper [Sta99], which makes direct use of the correlation function of the height field to compute the BRDF. Note that Stam’s formulation uses an analytical form of the continuous Fourier transform of the correlation function. Here again, we extend it with our windowing approach to compute continuous DTFT terms from convolution of the DFT impulses with the Fourier transform for a circular disc of radius $50\mu\text{m}$, which corresponds to the circular aperture of $100\mu\text{m}$ for the diaphragm in front of the laser source. At equal exposure as for Figure 10(d), Figure 11(d) (left image) completely lacks the *secondary* horizontal bands which are visible in Figure 10(d). This is because the correlation function for the height field does not have sufficient variations along the Y axis and most of the energy for the corresponding Fourier transforms is concentrated at the origin, leading to a bright specular highlight. Figure 11(d) (rightmost image) shows that even at high exposure, the output of this implementation does not show *secondary* horizontal bands. It rather has a *secondary* vertical band of colours. This is qualitatively different from the observations.

We also compared our lookup shader and Stam’s correlation method numerically in MATLAB. To do this, we used a benchmark implementation that performs *coherence windowing* in the spatial domain and computes $P_{\text{DTFT}}(u/\lambda, v/\lambda)$ terms in Equation (4)

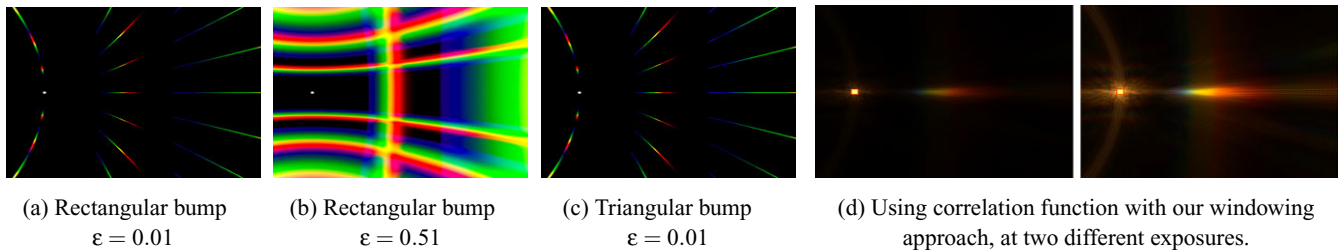


Figure 11: Simulation results for Stam's method for conditions matching our experimental verification setup for an *Elaphe* sample. (a)–(c) Correspond to Stam's implementation using the regular repetition of a 'basic bump' with periodicity matching the average size of an *Elaphe* 'nanofinger'. (a) and (b) Correspond to the rectangular bump depicted in Stam's paper [Sta99] with height and width as half of the respective periodicities. (c) Corresponds to the triangular bump depicted in Stam's paper [Sta99] (with its periodicity and the bounding-box equal to that of the rectangular bump). Images in (d) correspond to an implementation that uses Stam's formulation with the correlation function of the height field, with two different exposures.

Table 2: Mean error for various renderings in CIELAB colour space.

Exposure (in RU)	Error per pixel		Error ratio $E2/E1$
	Our method ($E1$)	Stam's method ($E2$)	
1	0.039	0.067	1.724
1000	4.295	7.843	1.826
7500	11.544	23.704	2.054

directly. Our benchmark implementation is the most accurate realization of Equation (4) and we use it to generate the *ground truth*. Numerical differences from the ground truth serves as our error measure. We emulate our experimental setup from Figure 8 in MATLAB with the diaphragm's aperture set to $65\mu\text{m}$ and the screen placed at 100 mm from the sample holder. We used an *Elaphe* sample of size $65\mu\text{m} \times 65\mu\text{m}$, layered with gold as discussed earlier. Using this setup, we render images of size 101×101 pixels for our lookup shader, Stam's correlation method and the benchmark implementation for error analysis. We use perceptually uniform CIELAB colour space to compare our and Stam's method perceptually. Since the mapping between the CIEXYZ and the CIELAB colour spaces is non-linear, we perform comparisons at three different exposures (expressed in equivalent RU units) to characterize the error differences between our and Stam's method. Table 2 shows error per pixel for both methods. Note that 1 unit of error corresponds to *just-noticeable-difference*. For longer exposures, mean error for our method is high, i.e. visual errors are noticeable, as it is also evident in our rendering in Figure 10(d) which corresponds to $7500RU$. However, these fairly noticeable visual differences are graceful degradations when compared to real-world observations. In comparison, for all the cases, the mean error for Stam's method is almost twice as that for our method. More importantly, the subjective qualification of the differences observed for Stam's method can be stated as significant perceptual departure from real-world observations (also evident in Figure 11 d). In conclusion, our biological samples do not respect the assumptions of Stam's diffraction shaders, and direct

use of Stam's method amounts to over-simplification of the complex nanostructures.

Stam has demonstrated that some previous BRDF models are special cases of his method. Let σ_h be the standard deviation for the height field and $g = (2\pi\sigma_h/\lambda)^2$. Stam [Sta99] shows that if $g \ll 1$ then his model can be simplified to the Born approximation and when $g \gg 1$, it can be simplified to using common BRDF models based on geometrical optics. In other words, using his model with a large number of Taylor series terms is justified only for cases with $g \approx 1$. While the complex nanostructures that we used cannot be modelled accurately as Gaussian random functions, they typically have $\sigma_h \approx 0.06\mu\text{m}$ and $g \approx 1$ for a representative wavelength of $\lambda = 500\text{nm}$. Similarly, our method as well needs a large number of Taylor series terms to converge.

7. Results

In this section, we examine and explain the output of our method for various nanostructures using BRDF maps. A BRDF map shows shader output for all viewing directions and a fixed incident light direction. Each view direction with spherical coordinates (θ_v, ϕ_v) is represented in the map at point $(x, y) = (\sin \theta_v \cos \phi_v, \sin \theta_v \sin \phi_v)$ with origin at the map-centre. We fix light direction for normal incidence, i.e. $(\theta_i, \phi_i) = (0, 0)$, unless it is specified otherwise. For visualization purpose, throughout this section, we use light intensity of $1500RU$, perform gamma correction with $\gamma = 2.2$ and apply sRGB colour gamut, unless it is specified otherwise.

Figure 12 shows BRDF maps output by our lookup shader for different nanostructures from Figure 5. The BRDF map for the blazed grating shows typical high relative brightness for the positive first order diffraction ($m = 1$) [PLT05], see Figure 12(b). Figure 12(c) corresponds to a synthetic CD disk nanostructure with random pits. Sharp diffraction of multiple orders across regularly placed CD tracks are noticed along the vertical axis for the map. This effect is due to fixed local periodicity of the tracks with high edge pit bumps. In contrast, there is only limited interference along arbitrary incident planes. The fact that randomly interleaved pits can only be of fixed possible lengths, 3–11 in bit units, exhibits some average

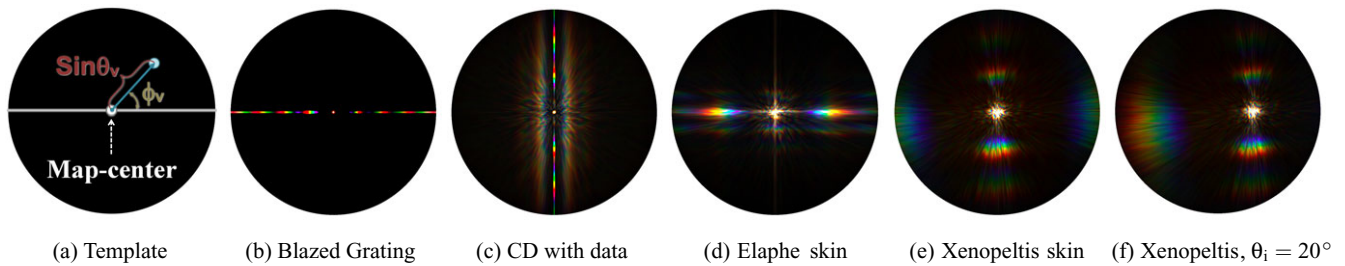


Figure 12: BRDF maps generated using our lookup shader. (b)–(e) Results for different nanostructures with normal incident light. (a) Illustrates the layout of BRDF maps where a viewing direction is represented distinctly in the map. For blazed gratings most of the diffracted spectral energy lies in first order ($m = 1$) for diffraction. The asymmetry is due to the asymmetric geometry of the grating (see Figure 5). (e) A BRDF map for *Xenopeltis* skin with $\theta_i = 20^\circ$, illustrating diffraction both along and across ‘nanofingers’.

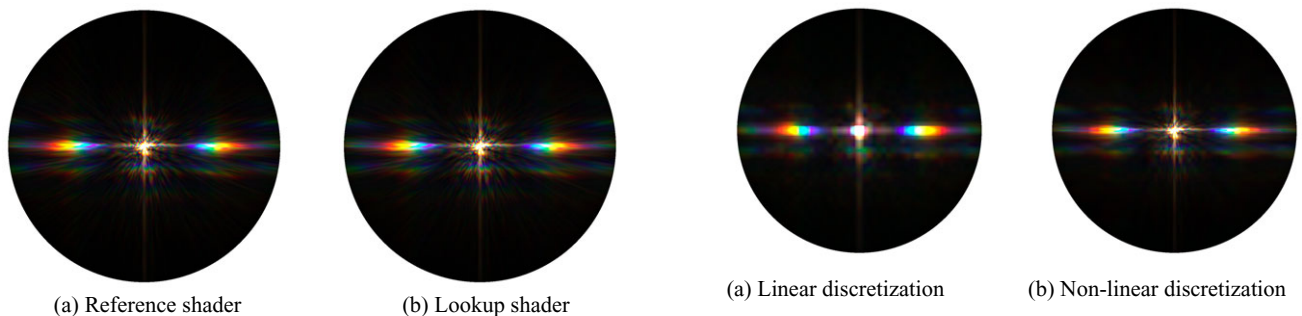


Figure 13: BRDF maps for comparison between reference and lookup shaders for the *Elaphe* nanostructure.

periodicity and we observe first order diffraction along many arbitrary directions.

For *Elaphe* skin, the finger-like nanostructures are quite regularly placed and it thus exhibits diffraction across these periodic arrangements, i.e. along the horizontal axis for the BRDF map in Figure 12(d). Furthermore, these ‘nanofingers’ overlap across layers and thus do not exhibit any definite periodicity along the finger direction. Hence, we do not see strong diffraction colours along other directions in the BRDF map. For *Xenopeltis*, the layers of ‘nanofingers’ do not overlap and they manoeuvre significantly along their length but with some local consistency. Thus, we observe diffraction along many different ‘almost vertical’ directions in our BRDF map in Figure 12(e). A similar argument holds true for diffraction across locally periodic finger patches with slightly different orientations. This diffraction across fingers is more conspicuous at an incident angle of 20° as shown in Figure 12(f).

We analysed the accuracy and behaviour of our lookup shader with subjective evaluations. To ascertain its accuracy we compared the lookup shader with the reference shader. Figure 13 confirms that the lookup shader output is visually similar to the reference-shader output. Figure 14 demonstrates that with equal number of (u, v) lookup samples, non-linear discretization of $u-v$ space outperforms linear discretization which produces an over-smoothed BRDF map. We observed the convergence for Taylor series summation in Equation (6) with an increase in the number of lookup

Figure 14: BRDF maps produced for *Elaphe* using lookup tables with (a) linear and (b) non-linear discretizations of the $u-v$ space with a resolution of 101×101 . Linear discretization results in an over-smooth BRDF map.

tables, see Figure 15. Note that though the results in Figures 15(b) and (e) look similar, they differ significantly in relative strength of the reflectances for the vertical diffraction modes. While Figure 15(b) has equal relative reflectances for all respective vertical diffraction modes, Figure 15(e) has lower reflectance strength for the vertical diffraction modes above the centre as compared to the ones below, see insets for Figures 15(b) and (e). This is typical for blazed gratings and *Xenopeltis* ‘nanofingers’ have vertical height profiles which are similar to that for a blazed grating. This subjective evaluation provides a visual justification for the use of many Taylor series terms. In theory, Taylor series of a bounded complex exponent (Equation 5) converges uniformly and the radius of convergence is infinite.

We studied the impact of coherence length by experimenting with the Gaussian window size σ_s . The output of the reference shader for the blazed grating with different σ_s values is shown in Figure 16. For smaller spatial windows there are fewer blaze periods participating in interference and hence produce less sharp colours. We also experimented with $\Delta\lambda$ for numerical integration in Equation (11) using our reference shader, see Figure 17 for results. For $\Delta\lambda \geq 10nm$, approximation errors for integration appear as artifacts in the BRDF map. For $\Delta\lambda = 5nm$, these artifacts become indiscernible and thus we generate lookup tables with $\Delta\lambda \leq 5nm$.

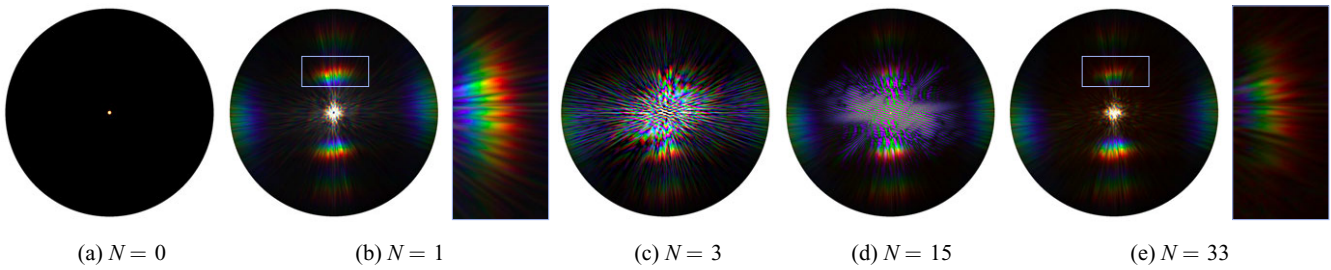


Figure 15: Convergence of the Taylor series with higher values for N in Equation (10) for the *Xenopeltis* nanostructure.

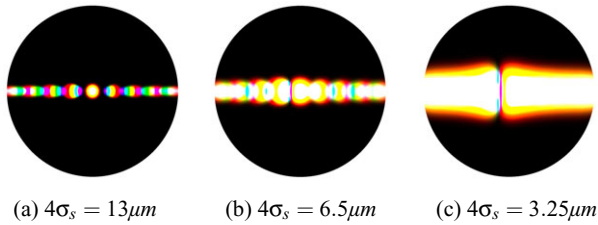


Figure 16: BRDF maps output by our reference shader for blazed grating for different coherence lengths for incident light. At lower coherence length, fewer interacting grating periods produce blurred diffraction bands for different λ which overlap to produce poorly resolved colours.

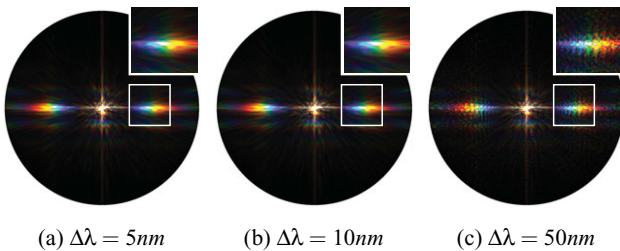


Figure 17: BRDF maps output by our reference shader for *Elaphe* using different $\Delta\lambda$ for numerical integration in Equation 11. For $\Delta\lambda \geq 10$ BRDF maps exhibit artifacts.

Lastly, we rendered a section of a real snake geometry for an *Elaphe guttata* with our lookup-renderer. The snake geometry was acquired along with skin-texture using photometric stereo. To compute diffraction colours on 3D surfaces we also need to define local orientations for the nanostructures. In reality, ‘nanofingers’ run parallel to snake scales (from the anterior end towards the posterior end of the animal) and we define an orientation field accordingly. To blend diffraction colours with texture we use the Fresnel term to estimate reflectance and transmittance of the incident light. We added an ambient light to the scene as well. Figure 1 shows rendering of the snake skin with and without texture and for two different light directions. We also rendered the same surface geometry without texture with the *Xenopeltis* nanostructure and show results in Figure 18(a). Diffraction colours change dramatically

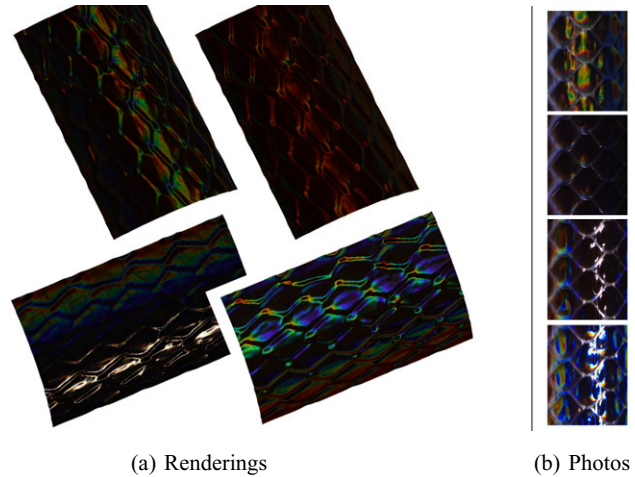


Figure 18: (a) Rendering the snake surface geometry with diffraction for *Xenopeltis* nanostructures using 800RU with different viewing and incidence directions. (b) Closeup photographs of *Xenopeltis* skin exhibiting stark iridescence under different illumination.

with changes in light direction, surface normals and viewing direction, which is typical for diffraction colours observed in nature, see Figure 18(b).

We evaluated run-time performance of our lookup shader using the FRAPS benchmarking tool [FRA13]. The screen resolution for the rendering window was set to 1024×1024 and we rendered the *Elaphe* snake geometry with texture-blending enabled. Our shader consistently crossed a benchmark of 120 fps for high user interactivity on an NVidia GTX680 GPU. In comparison, our reference shader (described in Section 5) has performance on the order of few seconds per frame when it uses pre-computed DFT coefficients with wavelength sampling at 5 nm.

8. Conclusions

We described a method for interactive rendering of diffraction due to complex, biological surface nanostructures. Our approach achieves interactive performance by pre-computing lookup tables using a Taylor series expansion and by including spectral integration in the pre-computation. We demonstrated our approach with two surface

structures acquired from snake sheds using AFM, and two synthetic test patterns. Our evaluation shows that our diffraction BRDFs are consistent with the behaviour of idealized gratings of similar periodicities, but exhibit more complex diffraction patterns because of the irregularities in biological structures. Beyond interactive rendering in computer graphics, we believe our approach will be useful as a tool for biologists to investigate the function and appearance of nanoscale structures on various organisms.

Acknowledgements

This work is supported by the Swiss National Science Foundation under the Sinergia program, grant number 132430. We thank Liana Manukyan and Michel Bessant from the LANE lab at the University of Geneva, for providing us with a 3D scanned, true surface mesh for an *Elaphe* snake.

References

- [BS63] BECKMANN P., SPIZZICHINO A.: *The Scattering of Electromagnetic Waves from Rough Surfaces*. Pergamon, New York, 1963.
- [CHB*12] CUYPERS T., HABER T., BEKAERT P., OH S. B., RASKAR R.: Reflectance model for diffraction. *ACM Transactions on Graphics* 31, 5 (Sept. 2012), 122:1–122:11.
- [CT82] COOK R. L., TORRANCE K. E.: A reflectance model for computer graphics. *ACM Transactions on Graphics* 1, 1 (Jan. 1982), 7–24.
- [FRA13] Frames-per-Second Benchmarking Tool (FRAPS). <http://www.fraps.com/>, 2013. Accessed 27 September 2013.
- [Gol13] Filmetrics : Refractive Index of Au, Gold. <http://www.filmetrics.com/refractive-index-database/Au/Gold>, 2013. Accessed 16 January 2014.
- [IOS*09] IMURA M., OSHIRO O., SAEKI M., MANABE Y., CHIHARA K., YASUMURO Y.: A generic real-time rendering approach for structural colors. In *VRST '09: Proceedings of the 16th ACM Symposium on Virtual Reality Software and Technology* (New York, NY, USA, 2009), ACM, pp. 95–102.
- [LA06] LINDSAY C., AGU E.: Physically-based real-time diffraction using spherical harmonics. In *Advances in Visual Computing*, G. Bebis, R. Boyle, B. Parvin, D. Koracin, P. Remagnino, A. Nefian, G. Meenakshisundaram, V. Pascucci, J. Zara, J. Molineros, H. Theisel, T. Malzbender (Eds.), vol. 4291, *Lecture Notes in Computer Science*. Springer, Berlin Heidelberg (2006), pp. 505–517.
- [Loe72] LOEBICH O.: The optical properties of gold. *Gold Bulletin* 5, 1 (1972), 2–10.
- [LSK05] LAZÁNYI I., SZIRMAY-KALOS L.: Fresnel term approximations for metals. In *WSCG (Short Papers)* (2005), pp. 77–80.
- [MGFG12] MASHAAL H., GOLDSTEIN A., FEUERMANN D., GORDON J. M.: First direct measurement of the spatial coherence of sunlight. *Optics Letters* 37, 17 (2012), 3516–3518.
- [MMRO13] MUSBACH A., MEYER G. W., REITICH F., OH S. H.: Full wave modelling of light propagation and reflection. *Computer Graphics Forum* 32, 6 (2013), 24–37.
- [OKG*10] OH S. B., KASHYAP S., GARG R., CHANDRAN S., RASKAR R.: Rendering wave effects with augmented light field. *Computer Graphics Forum* 29, 2 (2010), 507–516.
- [PLT05] PALMER C. A., LOEWEN E. G.: *Diffraction Grating Handbook*. Newport Corporation, Springfield, OH, USA, 2005.
- [Sta99] STAM J.: Diffraction shaders. In *SIGGRAPH '99: Proceedings of the 26th Annual Conference on Computer Graphics and Interactive Techniques* (New York, NY, USA, 1999), ACM Press/Addison-Wesley Publishing Co., pp. 101–110.
- [Sun06] SUN Y.: Rendering biological iridescences with rgb-based renderers. *ACM Transactions on Graphics* 25, 1 (Jan. 2006), 100–129.
- [TFNC01] TSINGOS N., FUNKHOUSER T., NGAN A., CARLBOM I.: Modeling acoustics in virtual environments using the uniform theory of diffraction. In *SIGGRAPH '01: Proceedings of the 28th Annual Conference on Computer Graphics and Interactive Techniques* (New York, NY, USA, 2001), ACM, pp. 545–552.
- [WZ13] WU F.-k., ZHENG C.-w.: A comprehensive geometrical optics application for wave rendering. *Graphical Models* 75, 6 (2013), 318–327.
- [Xen] A Xenopeltis Snake Exhibiting Spectacular Iridescence. <http://www.pythonpete.com/luchistaya-zmeya-xenopeltis-unicolor/>. Accessed 11 Feb 2014.
- [ZCG08] ZIEGLER R., CROCI S., GROSS M.: Lighting and occlusion in a wave-based framework. *Computer Graphics Forum* 27, 2 (2008), 211–220.